Available online at www.sciencedirect.com
SCIENCE DIRECT
Journal of Photochemistry and Photobiology A: Chemistry 176 (2005) 68–77
Journal of Photochemistry and Photobiology A:Chemistry
www.elsevier.com/locate/jphotochem

The absorption cross-section and photochemistry of OIO

D.M. Joseph [a], S.H. Ashworth [b,**], J.M.C. Plane [a,*]

[a] School of Environmental Sciences, University of East Anglia, Norwich NR4 7TJ, UK
[b] School of Chemical Sciences and Pharmacy, University of East Anglia, Norwich NR4 7TJ, UK

Available online 17 October 2005

Abstract

The absolute absorption cross-section of OIO was measured from 558 to 578 nm by using cavity ring-down spectroscopy to measure the fraction of OIO removed following absorption of a laser pulse of known fluence. This procedure yields $\sigma_{OIO} = (1.51 \pm 0.18) \times 10^{-17}$ cm^2 at 567.93 nm, which is one of the prominent vibrational band peaks in the OIO spectrum. The recovery of ground-state OIO after a few microseconds indicates that, after excitation from the ground $^2B_1$ to the (first) excited $^2B_2$ state, OIO undergoes rapid internal conversion onto high vibrational levels of the $^2B_1$ state, followed by quenching collisions with the bath gas. A detailed kinetic model is used to show that the OIO yield from the IO self reaction is 0.31 ± 0.10 at 40 Torr and 293 K. The rapid removal of OIO in the reactor is explained by the recombination of atomic I and OIO with a rate constant of $(1.1 \pm 0.3) \times 10^{-10}$ cm^3 molecule^{-1} s^{-1}. Ab initio calculations combined with RRKM theory are used to show that this rate constant is consistent with the addition of the I atom to the central I, rather than either of the terminal O atoms. The unexpectedly fast disappearance of I atoms, and the corresponding formation of I_2, is explained by iodine oxides such as IO, OIO and I_2O_3 acting as chaperone molecules.

Keywords: Iodine oxides; OIO; Marine boundary layer; Cavity ring-down spectroscopy

1. Introduction

The atmospheric chemistry of iodine is potentially important in several ways, including the destruction of ozone [1–3], the activation of chlorine and bromine from sea-salt [2,4], the removal of nitrogen oxides in semi-polluted air masses [3], and the formation of ultrafine aerosol [5–7]. The major sources of iodine appear to be iodocarbons of biogenic origin such as CH_3I and CH_2I_2 which evade from the ocean [8], and I_2 which is released from macroalgae exposed at low tide [9]. Following photolysis of these species to yield atomic I, the iodine oxide radical (IO) is then formed by reaction with O_3, and has been observed at several locations in the coastal marine boundary layer (MBL) [9–11].

The iodine dioxide radical (OIO) is formed from the self reaction of IO,

$$IO + IO \rightarrow OIO + I \quad (1a)$$

$$IO + IO \rightarrow \text{other products (e.g., IOIO, IOOI or } 2I + O_2) \quad (1b)$$

which has a yield α (i.e. channel (1a)) of around 40% [12,13]. We have observed OIO in the temperate MBL at Cape Grim, Tasmania [14] and Mace Head, Ireland [9], using the technique of differential optical absorption spectroscopy (DOAS) operating in the 540–585 nm spectral region. During daytime the OIO concentration was consistently below the detection limit (≈2 parts per trillion (ppt), using the new absolute cross-section determined in this paper). If the absence of OIO during the day is caused by rapid photolysis, then the O_3 destruction potential of the radical depends crucially on the pathway:

$$OIO + h\nu \rightarrow I + O_2 \quad (2a)$$

$$OIO + h\nu \rightarrow IO + O(^3P) \quad (2b)$$

Channel (2a) would enhance O_3 depletion, since the combination of reactions (1) and (2a) removes *two* O_3, whereas channel (2b) would lead to a null cycle.

Several groups [12,15–17] have shown that OIO has a strong absorption spectrum consisting of sequences of bands grouped in

* Corresponding author. Tel.: +44 1603 593108; fax: +44 1603 593127.
** Corresponding author. Tel.: +44 1603 593893; fax: +44 1603 592003.
E-mail addresses: s.ashworth@uea.ac.uk (S.H. Ashworth), j.plane@uea.ac.uk (J.M.C. Plane).

1010-6030/$ – see front matter © 2005 Elsevier B.V. All rights reserved.
doi:10.1016/j.jphotochem.2005.09.003

triplets between 480 and 645 nm. However, the bond dissociation energy for OI–O has been calculated from quantum theory to be $288 \pm 16\,kJ\,mol^{-1}$ [18], corresponding to a photo-dissociation threshold via channel (2b) of about 415 nm. Indeed, O atoms were not observed from the photolysis of OIO at 532 nm [16]. In contrast, channel (2a) is close to thermoneutral [17,18], so that absorption in these visible bands could lead to I atom production, although an upper limit to the efficiency for I atom production of only 0.15 was recently reported [16]. We are not aware of any attempt to observe the O_2 product, which might be produced in either the $^3\Sigma_g^-$ or $^1\Delta_g$ states [17].

We have previously described a high-resolution spectroscopic study of the visible bands of OIO from 542 to 605 nm [17]. The absence of rotational structure in the absorption spectrum, and the lack of a laser-induced fluorescence spectrum, led us to conclude that absorption leads to photolysis via channel (2a). This appeared to be supported by ab initio quantum calculations showing that the visible absorption bands arise from strongly allowed transitions from the ground $^2B_1$ state to the first $^2B_2$ state. Photolysis would then result from intersystem crossing onto surfaces correlating with $I + O_2(^3\Sigma_g^-$ or $^1\Delta_g)$ [17].

Here, we re-examine this conclusion by showing that although OIO is removed immediately after photo-absorption, enabling the absolute absorption cross-section to be determined, at longer times essentially all the OIO reappears. This is consistent with fast interconversion onto high vibrational levels of the ground electronic state, followed by quenching. From this, we conclude that the photolysis yield (reaction (2a)) is very small. A comprehensive kinetic model is then used to model the observed time dependence of OIO in these experiments. From this, we obtain a new estimate for the branching ratio to produce OIO in reaction (1), and also show that the fast decay of OIO in the absence of O_3, which has been observed in previous studies [13,16], is most likely explained by the recombination of OIO and atomic I.

2. Experimental

The photochemistry of OIO was studied using the pulsed laser photolysis/cavity ring-down (CRD) apparatus illustrated in Fig. 1. The ring-down cavity was incorporated into a slow flow reactor, with the cavity end mirrors placed in vacuum-tight gymbal mounts. The high reflectance mirrors (reflectance >0.999 at $\lambda = 565$ nm and 2 m radius of curvature) defined a 1.55 m long cavity. The ring-down time for the empty cavity was typically $\tau_0 = 750$ ns. This was routinely recorded at the start of a set of experiments and the standard deviation of τ_0 for an average of ten laser shots was consistently less than 1%. A quartz entrance window for the photolysis lasers was offset from the main axis. This arrangement provided an overlap between the CRD and photolysis lasers in the reaction zone of about 0.4 m. The end sections of the cell attached to the mirror mounts included inlets for "curtain" flows of N_2, which were directed towards the cavity mirrors to protect them from particle deposition or damage from the reactants.

The ring-down signal was generated using a Nd:YAG pumped dye laser (dye laser 1), tunable over the range 555–585 nm with Rhodamine 590 dye. The light leaking out of the far end of the cavity was detected with a photomultiplier tube after passing through a 485 nm long-pass filter. The ring-down signal was captured using a digital oscilloscope (LeCroy LT262 350 MHz bandwidth, 1 GS/s or LeCroy 9361C 300 MHz band-

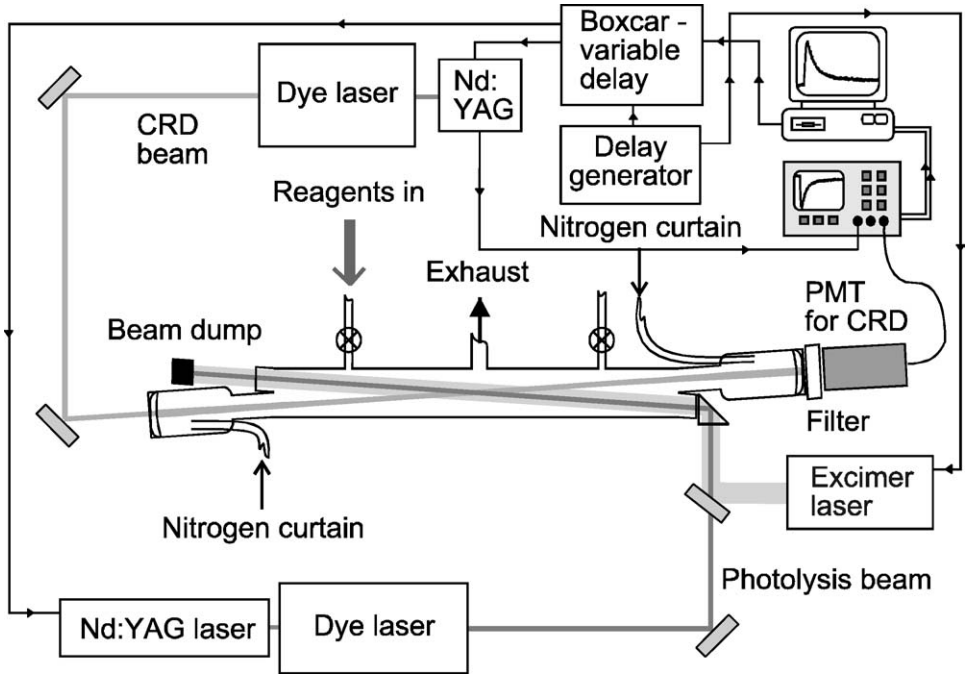

Fig. 1. Schematic diagram of the apparatus used to produce OIO by pulsed photolysis of a N_2O/CF_3I mixture, with detection by time-resolved cavity ring-down spectroscopy.

width, 2.5 GS/s), coupled to a computer which extracted the ring-down time constant using a weighted fit to the exponential decay and performed signal averaging. The absorbance due to OIO and I_2 (which absorbs in the same spectral region) is proportional to the difference between the ring-down time constant measured in the presence of OIO, and the ring-down time constant collected with just N_2 in the cell. Before the dye laser beam entered the CRD cell, a fraction was picked off with a wedged quartz beamsplitter and directed into an I_2 fluorescence cell and a Coherent Wavemaster for wavelength calibration.

OIO was generated from the self reaction of IO (reaction (1a)). IO was prepared by the pulsed photolysis of N_2O (Air Products, Atomic Absorption Grade) by an ArF excimer laser at 193 nm. This yields $O(^1D)$ atoms, which are rapidly quenched to $O(^3P)$ by collision with the N_2 bath gas. $O(^3P)$ then reacted with an excess of CF_3I (Fluorochem Ltd., 99%) to yield IO, and hence OIO. Typical experimental conditions were $[CF_3I] = 3.2 \times 10^{16}$ molecule cm^{-3}, $[N_2O] = 1.6 \times 10^{17}$ molecule cm^{-3}, $[N_2] = 1.2 \times 10^{18}$ molecule cm^{-3} (total pressure = 40.3 Torr). The excimer laser fluence at 193 nm was varied from 0.8 to 1.7×10^{16} photon cm^{-2}.

When measuring the absorption cross-section of OIO, the OIO was interrogated using a second Nd:YAG pumped dye laser (dye laser 2), also operating with Rhodamine 590 and beam-expanded to a diameter of 20 mm. Both dye lasers employed in this experiment had bandwidths of 0.2 cm^{-1} or better. This laser was triggered around 100 μs after the excimer laser when the OIO concentration had maximised, and was scanned over the region 558–578 nm. The degree of OIO removal following dye laser 2 was measured by monitoring the OIO ground-state concentration, using CRD with dye laser 1 fixed at 567.808 nm. This monitoring wavelength was selected to minimise interference from I_2, which absorbs over the same region and is generated by recombination of I atoms (see below). The OIO concentration was monitored at various time delays after dye laser 2, ranging from 300 ns to 10 μs. Because of the temporal behaviour of OIO after absorption (see Section 3.1), the OIO concentration was monitored at the shortest possible delay (300 ns) when measuring the OIO absorption cross-section.

The fluence of dye laser 2, which is required to determine the absorption cross-section, was measured at several points across the dye tuning curve with a Molectron Power Max power meter, through a 10 mm diameter aperture. The fluence data was then interpolated across the tuning curve by fitting to a second-order polynomial. The calibration of the power meter was compared with a second identical meter, as well as a Molectron J50 pyro-electric joulemeter. All three meters agreed within 5%.

In a limited set of experiments, the time-resolved behaviour of IO was monitored by laser-induced fluorescence (LIF). IO was excited at 444.951 nm [$IO(A^2\Pi_{3/2}–X^2\Pi_{3/2})$, (2,0)] using a dye laser with Coumarin 2 dye, pumped by a tripled Nd:YAG laser at 355 nm. The non-resonant LIF signal at 458.6 nm [$IO(A^2\Pi_{3/2}–X^2\Pi_{3/2}$, (2,1)] was recorded by a fast photomultiplier tube perpendicular to the CRD axis, after passing through a 455 nm long wave pass filter, and recorded using the digital oscilloscope. The time-resolved variation of atomic I was monitored by resonance fluorescence at 178.3 nm [$I(5p^4 6s(^2P_{3/2})–5p^5(^2P_{3/2})$] using a microwave-powered iodine discharge lamp. The fluorescence was measured with a photomultiplier tube after passing through an interference filter at 180 nm, and captured by photon-counting with a multichannel scaler. The resonance lamp and photomultiplier tube were mutually orthogonal to the CRD cell. Both the input and output optical trains were flushed with N_2 to allow transmission in the vacuum ultra-violet.

3. Results and discussion

3.1. OIO photolysis cross-section

The absolute cross-section for OIO absorption can be obtained by dividing the fraction of OIO removed, when laser 2 is triggered, by the measured fluence of the laser: in the limit of weak absorption, application of the Beer–Lambert law gives

$$\Delta[\mathrm{OIO}] \approx [\mathrm{OIO}]_0 \sigma_{\mathrm{OIO}} F \quad \text{(I)}$$

where $\Delta[OIO]$ is the change in OIO concentration when laser 2 triggers, $[OIO]_0$ the OIO concentration before laser 2 triggers, σ_{OIO} the absolute cross-section of OIO and F is the fluence of laser 2. Thus,

$$\sigma_{\mathrm{OIO}} = \frac{\Delta[\mathrm{OIO}]}{[\mathrm{OIO}]_0} \frac{1}{F} \quad \text{(II)}$$

The major advantage of using Eq. (II) is that the *absolute* concentration of OIO is not required to determine σ_{OIO}, only the fraction removed, $\Delta[OIO]/[OIO]_0$. However, in these experiments the fraction of OIO removed approached 30%, and so the weak absorption limit is not strictly applicable and Eq. (II) leads to σ_{OIO} being underestimated by about 6%. This was corrected for by iteratively fitting σ_{OIO} to the observed fraction of OIO removed. Fig. 2 shows the resulting absorption cross-section, which is the mean of four scans of laser 2 from 558 to 578 nm. The uncertainty in the cross-section, also shown in Fig. 2, is calculated from the standard deviation when averaging the spectra, combined with the uncertainty of F. At 567.93 nm,

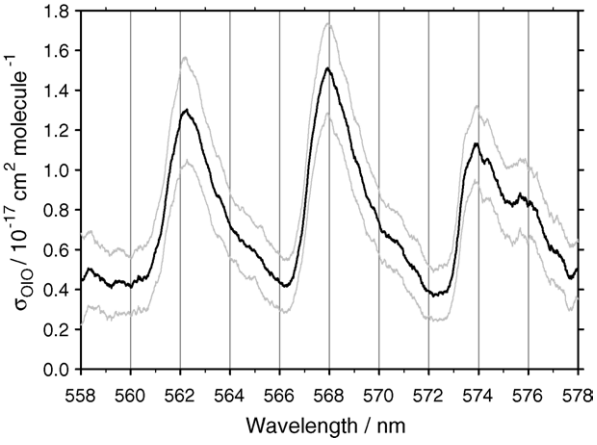

Fig. 2. The absolute absorption cross-section of OIO between 558 and 578 nm (black line), with 1σ error upper and lower limits (grey lines). Both pump and probe lasers have bandwidths better than 0.2 cm^{-1}.

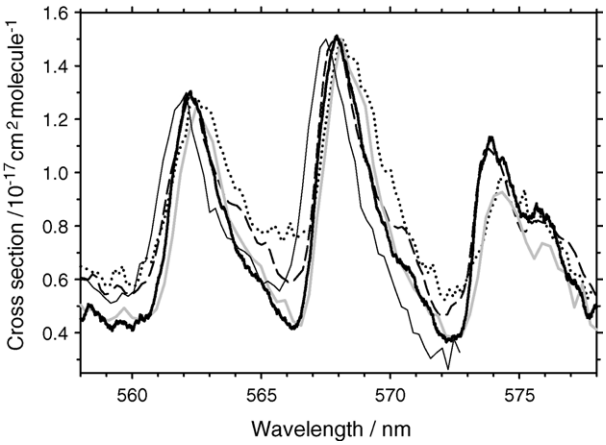

Fig. 3. The absolute absorption cross-section of OIO between 558 and 578 nm measured in the present study with a resolution of better than 0.2 cm^{-1} (thick solid black line), compared with previous spectra scaled to a value of 1.5×10^{-17} cm^2 molecule^{-1} at the 568 nm peak: Himmelmann et al. [15] (broken black line), Cox et al. [19] (thin solid black line), Ingham et al. [16] (dotted line), Gomez Martin and Spietz, University of Bremen (solid grey line).

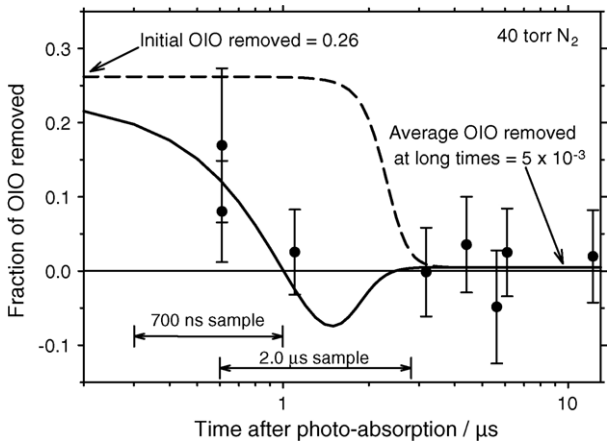

Fig. 4. Fraction of OIO removed following absorption at 562 nm, as a function of time after the laser pulse. The broken line shows a Monte-Carlo model prediction of the recovery of ground-state OIO, using the exponential-down model with $\langle \Delta E_{down} \rangle = 120\,cm^{-1}$. Because repopulation of the ground state occurs on a similar timescale to the ring-down time, the recovery that would have been observed experimentally is shown by the thick solid line, which should be compared directly with the experimental points. These points show the fraction of OIO removed at the time after the photo-excitation pulse when the CRD laser was triggered. The horizontal arrows indicate the two CRD sample lengths of 700 ns and 2 μs used in these experiments when observing at their respective shortest times (300 and 600 ns) after the photo-excitation pulse.

which is one of the prominent band peaks in the spectrum, $\sigma_{OIO} = (1.51 \pm 0.18) \times 10^{-17}$ cm^2, at a resolution of ~0.006 nm. This is in good agreement with the absorption cross-section of $(1.3 \pm 0.2) \times 10^{-17}$ cm^2 at a resolution of 0.35 nm determined by P. Spietz and J.-C. Gomez Martin at the University of Bremen (see accompanying paper in this issue).

Fig. 3 compares the OIO cross-section from the present study with absorption cross-section spectra reported by Himmelmann et al. [15], Cox et al. [19], Ingham et al. [16] and the new cross-section from University of Bremen. The spectra have been scaled so that their band peaks around 568 nm match the present study (note that the Cox et al. spectrum is blue-shifted by about 0.4 nm with respect to the other four). Compared with the UEA spectrum, the spectra of Himmelmann et al. and Ingham et al. (in particular) exhibit significantly greater absorption around 559.0, 561.5 and 572.5 nm, in between the vibrational bands. This is most likely due to an underlying absorption by I_2 in these spectra. As noted above, the CRD wavelength in the present study was set to 567.808 nm to minimise I_2 absorption. The new Bremen absorption spectrum has I_2 removed by a multi-dimensional fitting routine in wavelength and time (P. Spietz and J.-C. Gomez Martin, University of Bremen), and Fig. 3 shows that this spectrum agrees much better with the UEA spectrum.

The absorption cross-section in the present experiments (Fig. 2) was measured by fixing the time delay between laser 2 and the CRD laser to 300 ns. In a second set of experiments, OIO loss was measured at longer time delays after laser 2. These experiments show that after about 3 μs the OIO concentration completely recovers. That is, the fraction of OIO removed decreases essentially to zero (0.5%), as shown in Fig. 4. The recovery of OIO can be rationalised in terms of fast internal conversion from the excited $^2B_2$ state onto high vibrational levels of the $^2B_1$ ground state, followed by collisional relaxation which repopulates the ground state.

The CRD spectra of the OIO vibrational bands certainly indicate that OIO($^2B_2$) is short-lived: the linewidths of the bands are consistent with an upper state lifetime of no more than 500 fs. Band contour fits, using rotational constants for OIO($^2B_1$) from a microwave study [20], and approximate constants for the upper $^2B_2$ state from our ab initio calculations [17], show that the Lorentzian component of the rotational lines making up these bands is between 10 and 50 cm^{-1}. Following interconversion, the vibrationally excited OIO would have to lose about 17800 cm^{-1} to return to the ground state and be observed in absorption by the CRD laser.

The recovery of ground-state OIO can be simulated by a Monte-Carlo calculation using the exponential-down energy transfer model [21]. Because the ground state of OIO is repopulated on a similar timescale to the ring-down time, the predicted variation of OIO as a function of time must be converted to the ring-down time that would have been observed in the experiment, before comparison with the experimental points. The best fit to the experimental data is obtained with $\langle \Delta E_{down} \rangle = 120\,cm^{-1}$, as is shown by the solid line in Fig. 4. This value of $\langle \Delta E_{down} \rangle$ is a bit small for N_2 [21], but the exponential-down model is probably a rather crude description of energy transfer over such a large energy range. The broken line in Fig. 4 illustrates the actual recovery of OIO without including the effect of the ring-down time.

One point to note is that repopulation of the ground state perturbs the signal in such a way that the apparent ring-down time makes the absorption between 1 and 2 μs appear greater than when there is no removal of OIO. This effect can be visualised by considering a system which undergoes 100% removal followed by 100% recovery with the recovery on a time scale shorter than a single ring-down event. When the probe delay is such that the recovery takes place within the ring-down there is no longer a simple exponential curve. The ring-down is

initially at the empty cavity rate and finally at the rate consistent with 100% absorption. Between these two extremes the gradient is steeper than at either end and a simple weighted exponential fit to ring-down signals of this form distorts the retrieved ring-down time, making it appear that the absorption is higher than physically feasible. Perturbation of the ring-down time was investigated numerically by calculating the perturbed ring-down at successively longer delay times from the photo-excitation pulse using the modelled repopulation kinetics and extracting the ring-down using the same routine as in the acquisition program. Zero delay between photo-excitation and ring-down laser pulses corresponds to the ring-down measurement starting at the same time as the photo-excitation. The length of the ring-down recorded in these experiments (~2 μs) means that the reappearance of OIO in the ground state perturbs the decay even at short times after photo-absorption. Fig. 4 also shows that the OIO absorption cross-section measured at 300 ns would have been underestimated by about 19%.

It is important to note, however, that the absorption spectrum in Fig. 2 was recorded using a shorter portion of the ring-down – 700 ns – rather than almost 2 μs in subsequent experiments. In order to take this into account we ran the model again to produce the equivalent of the solid curve in Fig. 4 using only the first 700 ns of the ring-down decay. In this case, the repopulation dynamics do not have such a marked effect at short delays between the photo-excitation and ring-down acquisition, so that the effect on our absolute absorption cross-section would have been less than 5%, well within the quoted uncertainty. This is illustrated in Fig. 4 by the horizontal line showing the 700 ns sample interval starting 300 ns after the photo-excitation pulse. Comparison with the OIO recovery (broken line) shows that almost no OIO would have reappeared during this sampling interval.

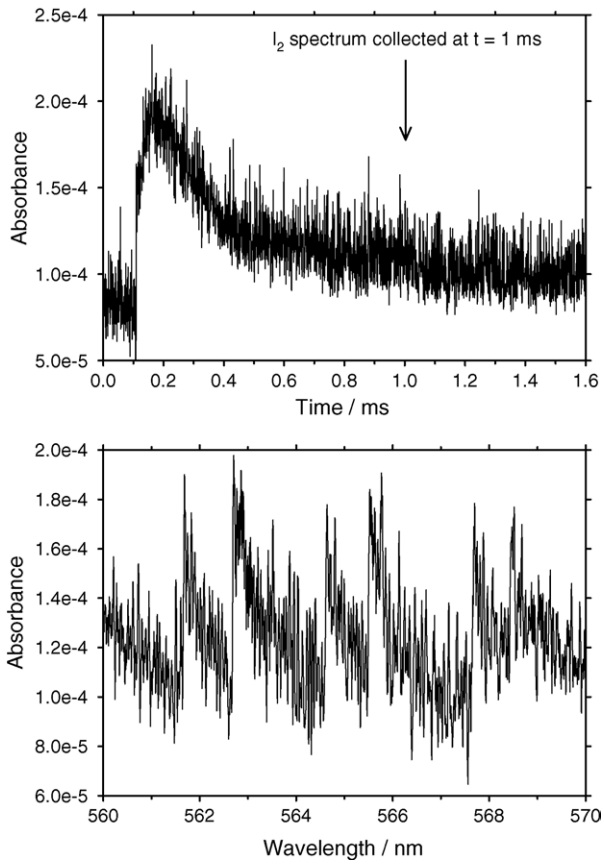

Fig. 5. Upper panel: cavity ring-down absorbance data at 567.81 nm, showing the time-profile of OIO and I_2 over 1.6 ms. Lower panel: a wavelength scan at 1.0 ms, taken 0.9 ms after the excimer laser pulse (at 0.1 ms), shows bands of I_2 and no evidence of OIO remaining in the cell.

3.2. Kinetic modelling of the temporal behaviour of OIO, I and I_2

3.2.1. Description of the model

Fig. 5 (top panel) illustrates the typical raw time-resolved variation of the CRDS absorbance at 567.81 nm. Most of the variation in the signal is due to the production and removal of OIO. There are two points to note. First is that while the rapid rise of OIO is expected because reaction (1a) is fast, the rapid decay after about 100 μs, which is approximately first-order with a decay rate that varied from 1800 to 6400 s^{-1} depending on the excimer laser fluences employed, is less easily accounted for. Such behaviour has been observed previously in similar systems [13,22]. Second is that there is residual absorbance after 1 ms, compared with before the excimer laser flash at $t = 0.1$ ms. The lower panel of Fig. 5 shows a spectral scan made at a time delay of 0.9 ms after the excimer flash. Comparison with Fig. 2 shows that the OIO bands have completely disappeared, and have been replaced with the absorption spectrum of I_2. Note that the growth of I_2 with a time constant of less than 1 ms is much faster than the recombination of I atoms in the presence of N_2, even making appropriate allowance for the greater third-body efficiencies of CF_3I, N_2O and I_2 itself compared with N_2. At much longer times (>10 ms after the excimer laser), the I_2 mixes radially in the reaction cell and the absorbance decreases to the pre-flash level.

We now apply a detailed kinetic model to explore both the fast decay of OIO and the rapid appearance of I_2. The model reaction scheme is listed in Table 1, there are 38 reactions involving 28 species, whose time-dependent concentrations are solved using fourth-order Runge–Kutta integration. For the products of the IO self reaction (reaction (1)), we assume that only two channels are important at the relatively low pressure of 40 Torr, formation of OIO + I and 2I + O_2. There is recent evidence that formation of the IOIO dimer only becomes significant at pressures above 150 Torr (P. Spietz and J.-C. Gomez (University of Bremen), T.J. Dillon and J.N. Crowley (MPI Mainz), pers. comm.), and there is consensus that the I_2 + O_2 channel branching ratio is less than 5% [13,19,23,24]. The photolysis cross-sections at 193 nm of N_2O, NO_2, CF_3I and I_2 were taken as 8.95×10^{-20} [25], 2.5×10^{-19} [26], 2×10^{-21} [27] and 1.92×10^{-17} [28] cm^2 $molecule^{-1}$, respectively at 295 K.

In order to compare the model with the experimental data, the experimental CRD absorbance was converted to the apparent OIO concentration using the cross-section determined above, and the I_2 concentration predicted by the model was converted to equivalent OIO concentration, using the relative cross-sections

Table 1
Model reaction scheme used to obtain α_{OIO} and k_{OIO+I}

Reactions	BR[a]	Rate coefficient[b]	Ref.
IO + IO → OIO + I (1a) IO + IO → 2I + O_2 (1b)	Fitted (0.31) (0.68)	$4.1 \times 10^{-11}\ e^{(220/T)}$	[13]
$O(^3P)$ + CF_3I → IO + CF_3 (3)		$1.3 \times 10^{-11}\ e^{(-266/T)}$	[37]
IO + NO_2(+M) → $IONO_2$ (4)		$k_0 = 7.7 \times 10^{-31}\ (T/300)^{-5}$, $k_\infty = 1.6 \times 10^{-11}$, $F_c = 0.4$	[38]
IO + NO → I + NO_2 (5)		$9.1 \times 10^{-12}\ e^{(240/T)}$	[25]
I + NO_2 (+M) → INO_2 (6)		$k_0 = 3.0 \times 10^{-31}\ (T/300)^{-1}$, $k_\infty = 6.6 \times 10^{-11}$, $F_c = e^{(-T/650)} + e^{(-2600/T)}$	[38]
I + NO (+M) → INO (7)		$k_0 = 3.0 \times 10^{-31}\ (T/300)^{-1}$, $k_\infty = 6.6 \times 10^{-11}$, $F_c = e^{(-T/650)} + e^{(-2600/T)}$	[39]
INO + INO → I_2 + 2 NO (8)		$8.4 \times 10^{-11}\ e^{(-2620/T)}$	[39]
INO_2 + INO_2 → I_2 + 2NO_2 (9)		$2.9 \times 10^{-11}\ e^{(-2600/T)}$	[39]
O + IO → O_2 + I (10)		1.35×10^{-10}	[40]
O + I_2 → IO + I (11)		1.4×10^{-10}	[25]
I + I (+M) → I_2 (12)		$6.1 \times 10^{-34} (T/298)^{0.073}\ e^{(894/T)}$	[41]
O + NO_2 → NO + O_2 (13a) O + NO_2 (+M) → NO_3 (13b)		$5.6 \times 10^{-12}\ e^{(180/T)}$, $k_0 = 9.0 \times 10^{-32}\ e^{(-2600/T)}$, $k_\infty = 6.6 \times 10^{-11}$, $F_c = 0.6$	[25]
N_2O + $O(^1D)$ → 2NO (14a) N_2O + $O(^1D)$ → N_2 + O_2 (14b)	0.58 0.42	1.2×10^{-10}	[25]
N_2 + $O(^1D)$ → N_2 + $O(^3P)$ (15)		$1.8 \times 10^{-11}\ e^{(110/T)}$	[25]
O + NO (+M) → NO_2 (16)		$k_0 = 9.0 \times 10^{-32}\ (T/298)^{-1.5}$, $k_\infty = 3.0 \times 10^{-11}$, $F_c = 0.6$	[25]
CF_3 + CF_3 → C_2F_6 (17)		3.9×10^{-12}	[42]
CF_3NO + O → Products (18)		$4.5 \times 10^{-12}\ e^{(-560/T)}$	[43]
CF_3 + $O(^3P)$ → CF_2O + F (19)		3.310^{-11}	[44]
CF_3 + NO_2 → CF_2O + FNO (20a) CF_3 + NO_2 → CF_2O + F + NO (20b)	0.98 0.02	1.75×10^{-11}	[45]
CF_3 + NO (+M) → CF_3NO (21)		$k_0 = 2.0 \times 10^{-29}\ (T/298)^{-3.3}$, $k_\infty = 2.0 \times 10^{-11}$, $F_c = 0.6$	[46]
CF_3 + O_2 (+M) → CF_3O_2 (22)		$k_0 = 3.0 \times 10^{-29}\ (T/298)^{-4}$, $k_\infty = 4.0 \times 10^{-12}\ (T/300)^{-1}$, $F_c = 0.6$	[25]
CF_3 + I (+M) → CF_3I (23)		$3.0 \times 10^{-11} (T/298)^{0.5}\ e^{(-200/T)}$	[47]
CF_3 + I_2 → CF_3I + I (24)		4.32×10^{-12}	[48]
CF_3 + N_2O → CF_3O + N_2 (25)		$2.32 \times 10^{-11}\ e^{(-12077/T)}$	[49]
CF_3 + O_3 → CF_3O + O_2 (26)		9.29×10^{-13}	[50]
CF_3 + CF_3I → C_2F_6 + I (27)		$<3.0 \times 10^{-16}$	[51]
CF_3O_2 + NO_2 (+M) → $CF_3O_2NO_2$ (28)		$k_0 = 2.2 \times 10^{-29}\ (T/298)^{-5}$, $k_\infty = 6.0 \times 10^{-12}\ (T/300)^{-2.5}$, $F_c = 0.6$	[25]
CF_3O + NO → CF_2O + FNO (29)		$3.7 \times 10^{-11}\ e^{(110/T)}$	[25]
CF_3O_2 + NO → CF_3O + NO_2 (30)		$5.4 \times 10^{-12}\ e^{(320/T)}$	[25]
F + CF_3I → CF_3 + IF (31)		1.2×10^{-10}	[52]
CF_3 + IO → CF_3O + I (32a) CF_3 + IO → CF_2O + IF (32b)	0.4 0.6	1.6×10^{-11}	[24,53]
OIO + NO → IO + NO_2 (33)		6.7×10^{-12}	[c]
I + IO (+M) → IOI (34)		2.2×10^{-12}	[d]
OIO + I (+M) → OI(I)O (35)		Fitted (1.1×10^{-10})	[d]
OIO + IO (+M) → I_2O_3 (36)		1.2×10^{-10}	[d]
I_2O_3 + I → $IIOIO_2$ (37)		1.0×10^{-10}	[d]
I + IOI → I_2 + IO (38a) I + OI(I)O → I_2 + OIO (38b) I + I(I)OIO_2 → I_2 + I_2O_3 (38c)		Single fitted value for (38a)–(38c) (9.0×10^{-12})	[e]

[a] Product branching ratio.
[b] *Units:* cm^3 $molecule^{-1}$ s^{-1} (bimolecular reactions), cm^6 $molecule^{-2}$ s^{-1} (termolecular reactions). For recombination reactions, k_0 is the low-pressure limiting rate constant; k_m is the high-pressure limiting rate constant; F_c is the broadening factor. The second-order recombination rate coefficient at total pressure [M] is given by $k_0[M]/(1 + k_0[M]/k_\infty)\ F_c^{\wedge}((1 + (\log_{10}(k_0[M]/k_\infty))^2)^{-1})$.
[c] Measured in this laboratory.
[d] Calculated from RRKM theory, using ab initio calculations on IOI and I_2O_3.
[e] Fitted to model the observed growth of I_2.

of OIO and I_2. Because of the high concentration of N_2O in the reactor, the cell is optically thick at 193 nm and the excimer laser fluence is reduced by 38% over the length of the part of the cell that is probed by the CRD laser. This effect is replicated in the model by dividing the reaction length into 1 cm intervals, and performing a separate integration of the chemistry in each one before the resulting time profiles are added to simulate the total absorbance. Another effect incorporated into the model is that the gas mixture experiences five excimer laser pulses as it flows through the portion of the tube where the excimer and CRD

lasers overlap. I_2 is therefore allowed to diffuse radially in the tube and build up between flashes, generating the background I_2 concentration that was observed experimentally immediately before each excimer laser flash. The various parameters that are fitted or estimated in the model are now discussed in turn.

3.2.2. The branching ratio to form OIO in the IO self reaction

The branching ratio to form OIO in reaction 1, α, is not well known. Previous published estimates are 0.38 ± 0.08 [13] and 0.44 ± 0.20 [24]. α can be estimated from the present experimental data without detailed knowledge of the reactions that remove OIO, because the OIO decay is very close to being first-order after about 200 μs. The rate of the IO self reaction can be calculated by using the measured excimer laser fluence to estimate the [IO] produced from photolysis of N_2O, and taking a recent measurement of k_1 [13]. The rate of OIO production is then this rate multiplied by α. Since the absolute [OIO] is obtained from the observed OIO absorption and σ_{OIO}, a simple balance between production and loss of OIO indicates that α is about 0.3. This value was used for the initial model runs to explore the decay of OIO and the production of I_2.

3.2.3. Removal of OIO

There are actually few candidate species with sufficient concentration in the reactor to remove OIO at the observed decay rate, since a first-order removal rate of $6000\,s^{-1}$ would require the species to have a concentration greater than about 3×10^{13} molecule cm^{-3}, and to persist for at least 700 μs after the excimer laser flash. The possible species are I, IO and CF_3 radicals. However, the time-resolved LIF observations of IO showed that this radical decayed at a faster rate than OIO, with an approximately first-order rate of $(1–1.5) \times 10^4\,s^{-1}$. Hence, this species does not persist long enough to be responsible for removing OIO at times longer than about 200 μs. On the other hand, the decay of atomic I is much slower, with an approximate first-order rate of $500–700\,s^{-1}$, making it a more likely candidate.

In order to explore which of these species could be responsible for the removal of OIO, we carried out ab initio quantum calculations to determine possible reaction pathways. The Gaussian 03 suite of programs [29] was used with a recently published basis set for I [30], and the standard 6-311 + g(2d,p) basis set for O, F and C. Following geometry optimization and the determination of vibrational frequencies, the following results were obtained (empirical spin–orbit splittings of −17 and $-5\,kJ\,mol^{-1}$ were applied to I and IO, respectively, by comparing the ab initio and the experimental bond energies of I_2 and IO):

$$I + OIO \rightarrow OI(I)O, \quad \Delta H_0 = -79\,kJ\,mol^{-1} \tag{35a}$$

$$I + OIO \rightarrow IOIO, \quad \Delta H_0 = -59\,kJ\,mol^{-1} \tag{35b}$$

$$IO + OIO \rightarrow I_2O_3, \quad \Delta H_0 = -122\,kJ\,mol^{-1} \tag{36}$$

$$CF_3 + OIO \rightarrow CF_3O + IO, \quad \Delta H_0 = -105\,kJ\,mol^{-1} \tag{39a}$$

$$CF_3 + OIO \rightarrow CF_3OI + O, \quad \Delta H_0 = -58\,kJ\,mol^{-1} \tag{39b}$$

The species OI(I)O in reaction (35a) describes a Y-shaped molecule where the I atom bonds to the central iodine atom in OIO, rather than IOIO (reaction (35b)) where the I atom bonds to one of the terminal oxygen atoms. The enthalpy changes in reactions (35a) and (35b) are in very good accord with the earlier calculations of Misra and Marshall [18]. Note that atomic I cannot abstract the central I in OIO directly to form $I_2 + O_2$. The transition state for this reaction at the B3LYP/6-311 + g(2d,p) level of theory is $65\,kJ\,mol^{-1}$.

Rate coefficients for the recombination reactions (35a), (35b) and (36) can be estimated from Rice–Ramsberger–Kassel–Markus (RRKM) theory. Here, we use the Master Equation (ME) formalism developed by De Avillez Pereira et al. [31]. Since we will show below that the recombination of I with OIO most likely accounts for the removal of OIO in our system, we describe the RRKM calculation on reaction (35a) in some detail. The reaction is assumed to proceed via the formation of an excited adduct ($OI(I)O^*$) which can either dissociate to OIO + I or be stabilized by collision with the third body (N_2). The adduct energy was divided into a contiguous set of grains (width $30\,cm^{-1}$), each containing a bundle of rovibrational states. Each grain was then assigned a set of microcanonical rate coefficients for dissociation, which were determined using inverse Laplace transformation (ILT) to link them directly to $k_{rec,\infty}$, the high pressure limiting recombination coefficient [31]. $k_{rec,\infty}$ was calculated using long-range capture theory [32], which is dominated by the dipole of OIO (3.89 D at the B3LYP/6-311 + g(2d,p) level of theory) and the polarizability of the iodine atom ($5.35 \times 10^{-24}\,cm^3$ [33]). $k_{rec,\infty}$ was then expressed in Arrhenius form, $A^\infty \exp(-E^\infty/RT)$ before application of the ILT formalism.

The density of states of the adduct was calculated using a combination of the Beyer–Swinehart algorithm for the vibrational modes (without making a correction for anharmonicity), and a classical densities of states treatment for the rotational modes [21]. The ab initio rotational constants for OI(I)O are 5.61, 0.807 and 0.750 GHz, and the vibrational frequencies are 128, 142, 209, 284, 852 and $886\,cm^{-1}$. The two very low frequencies, which correspond to out-of-plane and in-plane rocking modes of the OIO, were treated as a two-dimensional free rotor [21].

The ME describes the evolution with time of the adduct grain populations. The probability of collisional transfer between grains was estimated using the exponential down model [21], where the average energy for downward transitions, $\langle \Delta E_{down} \rangle$, was set to $500\,cm^{-1}$ for N_2 at 300 K, with a $T^{0.5}$ temperature dependence. The collision frequency between the adduct and N_2 was calculated using an intermolecular potential described by the parameters $\sigma = 5$ Å and $\varepsilon/k = 300$ K [34]. In order to use the ME to simulate irreversible stabilization of $OI(I)O^*$, an absorbing boundary was set $24\,kJ\,mol^{-1}$ below the energy of the reactants, so that collisional energization from the boundary to the threshold was highly improbable.

The ME was then solved to yield k_{rec}, the recombination rate constant, over a range of temperature (200–400 K) and pressure (0–1000 Torr). The results were fitted to the Lindemann

expression modified by a broadening factor F_c [21], yielding: $k_{rec,0} = 6.5 \times 10^{-28}$ $(T/300\,K)^{-2.54}$ cm^6 molecule^{-2} s^{-1}, $k_{rec,\infty} = 2.4 \times 10^{-10}$ exp$(-0.42\,kJ\,mol^{-1}/RT)$ cm^3 molecule^{-1} s^{-1} and $F_c = 0.48$. Under the conditions used in the present experiments (40 Torr and 293 K), $k_{rec} = 1.1 \times 10^{-10}$ cm^3 molecule^{-1} s^{-1}, so reaction (35a) is predicted to be close to the high pressure limit.

RRKM calculations on reaction (35b), treating the IOIO* adduct as having two internal free rotors, indicates that $k_{rec} = 2.9 \times 10^{-11}$ cm^3 molecule^{-1} s^{-1} at 40 Torr N_2 and 293 K. Reaction (35b) is slower than 35a because the binding energy of the I atom to one of the terminal O atoms is smaller than to the central iodine of OIO. RRKM calculations on reaction (36) indicate that this reaction is close to the high pressure limiting rate constant at 40 Torr and 293 K: $k_{rec} = 1.2 \times 10^{-10}$ cm^3 molecule^{-1} s^{-1}. Since this reaction cannot be primarily responsible for OIO removal (because of the observed rapid disappearance of IO), it was not treated as a variable parameter and set to this value in the kinetic model (Table 1). Finally, although there are two exothermic reaction channels for the reaction between CF_3 and OIO (reactions (39a) and (39b)), the products are IO and O (+$CF_3I \rightarrow$ IO), which would recycle back to OIO and not cause the rapid removal of OIO that is observed. We therefore conclude that reaction (35a) is the most likely cause for OIO removal in our system, and so the rate constant, k_{35a}, was treated as an adjustable parameter in the kinetic model.

3.2.4. Conversion of I to I_2

The rate of I_2 formation in the 1 ms interval after the excimer laser, and the decay of atomic I observed by resonance fluorescence, are not explained by termolecular recombination of I, even enhanced by the presence of CF_3I, N_2O and I_2 as third bodies. Following the suggestion of Harwood et al. [22], we therefore allowed the iodine oxides in the model to act as chaperones for I atom recombination. For example:

$$I + IO \rightarrow IOI, \quad \Delta H_0 = -103\,kJ\,mol^{-1} \tag{34}$$

$$I + IOI \rightarrow I_2 + IO, \quad \Delta H_0 = -46\,kJ\,mol^{-1} \tag{38a}$$

An RRKM calculation on reaction (34) indicates that $k_{rec} = 2.2 \times 10^{-12}$ cm^3 molecule^{-1} s^{-1} at 40 Torr N_2 and 293 K. The analogous cycles involving OIO and I_2O_3 are:

$$\text{Reaction (35a), then } I + OI(I)O \rightarrow I_2 + OIO, \quad \Delta H_0 = -70\,kJ\,mol^{-1} \tag{38b}$$

$$\text{Reaction (37), then } I + I(I)OIO_2 \rightarrow I_2 + I_2O_3 \tag{38c}$$

A single rate coefficient k_{38}, describing the abstraction of an I atom attached to any of these iodine oxides, was fitted as a variable parameter in the model.

3.2.5. Fitting the experimental data

The three fitted parameters in the kinetic model were thus α, k_{35a} and k_{38}. An example of a satisfactory model fit to the CRDS time-profile, judged by χ^2 minimisation, is illustrated in Fig. 6.

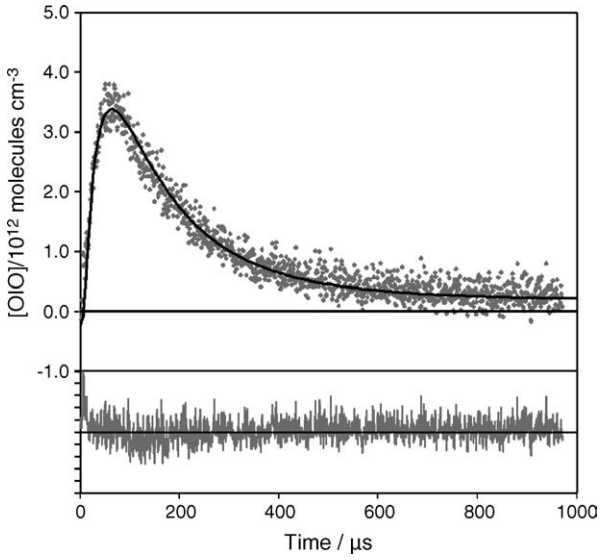

Fig. 6. Upper panel: cavity ring-down absorbance data converted to effective OIO concentration (grey dots), fitted by the kinetic model (black line). Lower panel: residuals between experiment and model, showing no systematic deviations.

Fig. 7 shows the time variation of all the iodine species predicted by the model. This confirms the tight coupling between IO and OIO; the rapid decay of IO means that reaction (37) cannot account for the near first-order removal of OIO. Note also the much slower disappearance of atomic I and corresponding rise of I_2.

The fits to the data were consistent in quality across the range of excimer laser fluence, Φ, employed. Furthermore, the best fit values of α and k_{35a} are within error independent of Φ. This is shown in Figs. 8 and 9, where the fluence varies by a factor of more than 2.

The average fitted values are $\alpha = 0.31 \pm 0.10$, and k_{35a} is $(1.1 \pm 0.3) \times 10^{-10}$ cm^3 molecule^{-1} s^{-1}. These uncertainties combine an estimated 10% uncertainty in the excimer laser fluence measurement, the 12% uncertainty in the OIO cross-section

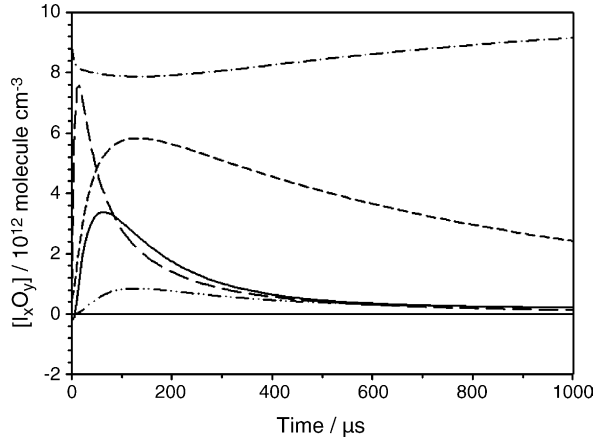

Fig. 7. Predicted time-profiles of five iodine species, following the 193 nm photolysis of a mixture of N_2O and CF_3I. The excimer laser fires at $t = 0$. The concentration profiles are: [OIO] (—), [IO]/10 (– –), [I]/10 (- -), [I_2]/10 (-·-·), [I_2O_3] (-··-··).

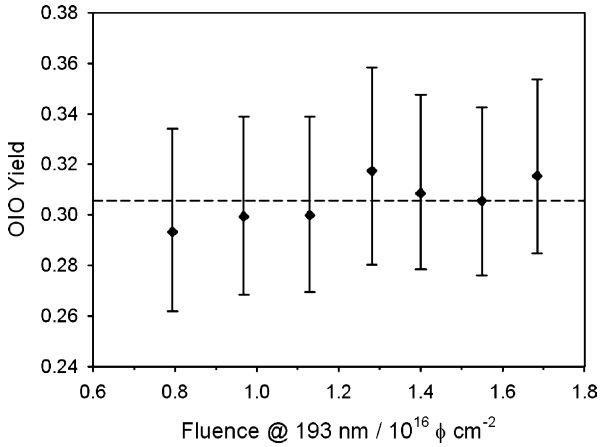

Fig. 8. Branching ratio α for OIO production from the IO self reaction, plotted against excimer laser fluence. The broken line indicates the average branching ratio. The determination of the error bars is described in the text.

(see above), and the smaller uncertainties in the photolysis cross-section of N_2O and the pertinent rate coefficients in Table 1 that lead to the production of IO, and the pressure and mass flow rates in the reaction cell. The value of α thus agrees within error with the two published values of 0.38 ± 0.08 [13] and 0.44 ± 0.20 [24]. It should be noted that these previous studies were made at 760 and 2 Torr, respectively, which may indicate that α is not very pressure-dependent. Furthermore, the best fit value of k_{35a} is in very good accord with the value calculated earlier using RRKM theory.

Finally, the best fit value of the rate constant describing the formation of I_2, by an I atom abstracting the weakly bound I atom from various iodine oxide–I atom adducts, is $k_{38} = 9.0 \pm 2.0 \times 10^{-12}$ cm^3 molecule^{-1} s^{-1}. The magnitude of this rate constant was determined from the fit of the tail of the CRD decay, where the observed absorption is mostly due to I_2. Note that since k_{38} is about an order of magnitude slower than k_{35a}, the OIO concentration is suppressed at longer reaction times, as observed experimentally.

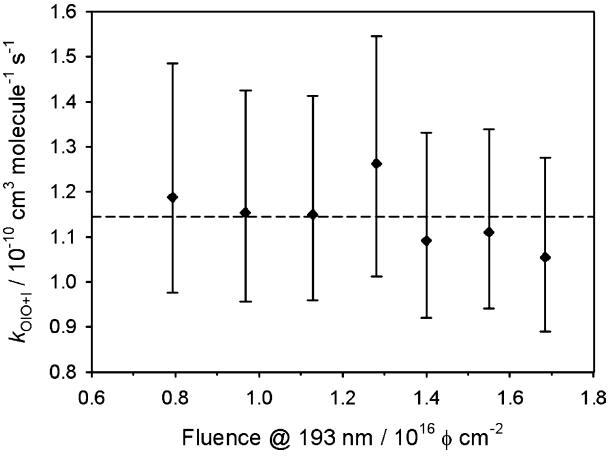

Fig. 9. Fitted rate constant for the reaction OIO + I → OI(I)O, plotted against excimer laser fluence. The average rate constant is indicated by the broken line. The error bar calculation is described in the text.

Of course, the treatment of the higher iodine oxides in this model is probably simplistic, since I_2O_3 may not be the terminal oxide, and polymerization must occur since there was a slow build up of a fine white solid on the interior wall of the reactor. Note that visible particle formation occurs much more readily if even a trace of O_3 ($\sim 1 \times 10^{15}$ cm^{-3}) is present. When the solid was removed and dissolved in distilled water, the solution was found to contain IO_3^- ions (A.R. Baker, University of East Anglia, pers. comm.). This indicates that the white deposit was I_2O_3, I_2O_5 or I_4O_9, as discussed originally by Cox and Coker [35].

4. Conclusions

The absolute absorption cross-section of OIO has been determined between 558 and 578 nm, using cavity ring-down spectroscopy and a method that requires the laser fluence rather than the absolute OIO concentration. Time-resolved measurements demonstrate the recovery of ground-state OIO on a timescale of a few microseconds, consistent with internal conversion of excited OIO and quenching by the bath gas. The upper limit for the photolysis yield of OIO at 562 nm is 10%, in accord with a previous upper limit derived from observing an insignificant yield of I atoms [16]. It should be noted that this result is consistent with the photochemistry of OClO, where the yield of $Cl + O_2$ is less than 4% between 365 and 450 nm [54].

Although a small amount of OIO photolysis may occur, these results indicate that the cycle involving production of OIO from the self reaction of IO (reaction (1a)), followed by photolysis to $I + O_2$ (reaction (2a)), should not play a significant role in ozone removal in the MBL. Instead, the stability of OIO against photolysis means that this molecule is probably of central importance in the formation of ultrafine iodine oxide particles, through the reaction of IO and OIO to form I_2O_3 [36]. A recent modelling study indicates that this reaction is fast enough to suppress the OIO concentration to below the detection limits of DOAS instruments, thus explaining the apparent absence of OIO during daytime when there are elevated concentrations of IO [36].

Acknowledgments

This work was supported by the UK Natural Environment Research Council under the *COSMAS* initiative, and by the *THALOZ* project funded by the European Commission.

References

[1] D.J. Davis, J. Crawford, S. Liu, S. McKeen, A. Bandy, D. Thornton, F. Rowland, D. Blake, J. Geophys. Res. 101 (1996) 2135–2147.
[2] R. Vogt, R. Sander, R. Von Glasow, P.J. Crutzen, J. Atmos. Chem. 32 (1999) 375–395.
[3] G. McFiggans, J.M.C. Plane, B.J. Allan, L.J. Carpenter, H. Coe, C. O'Dowd, J. Geophys. Res. Atmos. 105 (2000) 14371–14385.
[4] G. McFiggans, R.A. Cox, J.C. Mossinger, B.J. Allan, J.M.C. Plane, J. Geophys. Res. Atmos. 107 (2002) (Art. no. 4271).
[5] J.L. Jimenez, R. Bahreini, D.R. Cocker, H. Zhuang, V. Varutbangkul, R.C. Flagan, J.H. Seinfeld, C.D. O'Dowd, T. Hoffmann, J. Geophys. Res. Atmos. 108 (2003) (Art. no. 4318).

[6] G. McFiggans, H. Coe, R. Burgess, J. Allan, M. Cubison, M.R. Alfarra, R. Saunders, A. Saiz-Lopez, J.M.C. Plane, D.J. Wevill, L.J. Carpenter, A.R. Rickard, P.S. Monks, Atmos. Chem. Phys. 4 (2004) 701–713.
[7] C.D. O'Dowd, J.L. Jimenez, R. Bahreini, R.C. Flagan, J.H. Seinfeld, K. Hameri, L. Pirjola, M. Kulmala, S.G. Jennings, T. Hoffmann, Nature (2002) 632–636.
[8] L.J. Carpenter, G. Malin, P.S. Liss, F.C. Kupper, Glob. Biogeochem. Cycle 14 (2000) 1191–1204.
[9] A. Saiz-Lopez, J.M.C. Plane, Geophys. Res. Lett. 31 (2004) (Art. no. L04112).
[10] B.J. Allan, G. McFiggans, J.M.C. Plane, H. Coe, J. Geophys. Res. Atmos. 105 (2000) 14363–14369.
[11] B. Alicke, K. Hebestreit, J. Stutz, U. Platt, Nature 397 (1999) 572–573.
[12] R.A. Cox, W.J. Bloss, R.L. Jones, D.M. Rowley, Geophys. Res. Lett. 26 (1999) 1857–1860.
[13] W.J. Bloss, D.M. Rowley, R.A. Cox, R.L. Jones, J. Phys. Chem. 105 (2001) 7840–7854.
[14] B.J. Allan, J.M.C. Plane, G. McFiggans, Geophys. Res. Lett. 28 (2001) 1945–1948.
[15] S. Himmelmann, J. Orphal, H. Bovensmann, A. Richter, A. Ladstatter-Weissenmayer, J.P. Burrows, Chem. Phys. Lett. 251 (1996) 330–334.
[16] T. Ingham, M. Cameron, J.N. Crowley, J. Phys. Chem. A 104 (2000) 8001–8010.
[17] S.H. Ashworth, B.J. Allan, J.M.C. Plane, Geophys. Res. Lett. 29 (2002) (Art. no. 1456).
[18] A. Misra, P. Marshall, J. Phys. Chem. A 102 (1998) 9056–9060.
[19] R.A. Cox, W.J. Bloss, R.L. Jones, D.M. Rowley, Geophys. Res. Lett. 26 (1999) 1857–1860.
[20] C.E. Miller, E.A. Cohen, J. Chem. Phys. 118 (2003) 1–9.
[21] R.G. Gilbert, S.C. Smith, Theory of Unimolecular and Recombination Reactions, Blackwell, Oxford, 1990.
[22] M.H. Harwood, J.B. Burkholder, M. Hunter, R.W. Fox, A.R. Ravishankara, J. Phys. Chem. A 101 (1997) 853–863.
[23] S.P. Sander, J. Phys. Chem. 90 (1986) 2194–2199.
[24] A. Vipond, C.E. Canosa-Mas, M.L. Flugge, D.J. Gray, D.E. Shallcross, D. Shah, R.P. Wayne, Phys. Chem. Chem. Phys. 4 (2002) 3648–3658.
[25] S.P. Sander, R.R. Friedl, D.M. Golden, M.J. Kurylo, R.E. Huie, V.L. Orkin, G.K. Moortgat, A.R. Ravishankara, C.E. Kolb, M.J. Molina, B.J. Finlayson-Pitts, Chemical Kinetics and Photochemical Data for Use in Stratospheric Modelling: Evaluation 14, JPL Publication 02-25, Pasadena, 2002.
[26] A.M. Bass, A.E.J. Ledford, A.H. Lauffer, J. Res. NBS 80A (1976) 143–151.
[27] A. Fahr, A.K. Nayak, R.E. Huie, Chem. Phys. 199 (1995) 275–284.
[28] A. Saiz-Lopez, R.W. Saunders, M. Joseph, S.H. Ashworth, J.M.C. Plane, Atmos. Chem. Phys. 4 (2004) 1443–1450.
[29] M.J. Frisch, G.W. Trucks, H.B. Schlegel, G.E. Scuseria, M.A. Robb, J.R. Cheeseman, J.J.A. Montgomery, T. Vreven, K.N. Kudin, J.C. Burant, J.M. Millam, S.S. Iyengar, J. Tomasi, V. Barone, B. Mennucci, M. Cossi, G. Scalmani, N. Rega, G.A. Petersson, H. Nakatsuji, M. Hada, M. Ehara, K. Toyota, R. Fukuda, J. Hasegawa, M. Ishida, T. Nakajima, Y. Honda, O. Kitao, H. Nakai, M. Klene, X. Li, J.E. Knox, H.P. Hratchian, J.B. Cross, C. Adamo, J. Jaramillo, R. Gomperts, R.E. Stratmann, O. Yazyev, A.J. Austin, R. Cammi, C. Pomelli, J.W. Ochterski, P.Y. Ayala, K. Morokuma, G.A. Voth, P. Salvador, J.J. Dannenberg, V.G. Zakrzewski, S. Dapprich, A.D. Daniels, M.C. Strain, O. Farkas, D.K. Malick, A.D. Rabuck, K. Raghavachari, J.B. Foresman, J.V. Ortiz, Q. Cui, A.G. Baboul, S. Clifford, J. Cioslowski, B.B. Stefanov, G. Liu, A. Liashenko, P. Piskorz, I. Komaromi, R.L. Martin, D.J. Fox, T. Keith, M.A. Al-Laham, C.Y. Peng, A. Nanayakkara, M. Challacombe, P.M.W. Gill, B. Johnson, W. Chen, M.W. Wong, C. Gonzalez, J.A. Pople, Gaussian 03, Revision B. 03, Gaussian Inc., Pittsburgh, PA, 2003.
[30] M.N. Glukhovtsev, A. Pross, M.P. McGrath, L. Radom, J. Chem. Phys. 103 (1995) 1878–1885.
[31] R. De Avillez Pereira, D.L. Baulch, M.J. Pilling, S.H. Robertson, G. Zeng, J. Phys. Chem. 101 (1997) 9681.
[32] G.C. Maitland, M. Rigby, E.B. Smith, W.A. Wakeham, Intermolecular Forces Their Origin and Determination, Oxford University Press, Oxford, 1981.
[33] D.R. Lide, Handbook of Physics and Chemistry, CRC Press, Boca Raton, FL, 1992.
[34] J. Troe, J. Chem. Phys. 66 (1977) 4758–4765.
[35] R.A. Cox, G.B. Coker, J. Phys. Chem. 87 (1983) 4478–4484.
[36] A. Saiz-Lopez, J.M.C. Plane, G. McFiggans, S.M. Ball, M. Bitter, R.L. Jones, Atmos. Chem. Phys. Dissc. 5 (2005) 5405–5439.
[37] D. Hölscher, C. Fockenberg, R. Zellner, Ber. Bunsen Phys. Chem. 102 (1998) 716–722.
[38] G. McFiggans, J.M.C. Plane, B.J. Allan, L.J. Carpenter, H. Coe, C.D. O'Dowd, J. Geophys. Res. Atmos. 105 (2000) 14371–14385.
[39] W.B. DeMore, S.P. Sander, D.M. Golden, R.F. Hampson, M.J. Kurylo, C.J. Howard, A.R. Ravishankara, C.E. Kolb, M.J. Molina, Chemical Kinetics and Photochemical Data for Use in Stratospheric Modelling: Evaluation 12, JPL/NASA, Pasadena, 1997.
[40] C.E. Canosa-Mas, M.L. Flugge, D. Shah, A. Vipond, R.P. Wayne, J. Atmos. Chem. 34 (1999) 153–162.
[41] J.K.K. Ip, G.J. Burns, J. Chem. Phys. 56 (1972) 3155.
[42] A.B. Vakhtin, Int. J. Chem. Kin. 28 (1996) 443–452.
[43] R.P. Thorn, J.M. Nicovich, J.M. Cronkhite, S. Wang, P.H. Wine, Int. J. Chem. Kin. 27 (1995) 369–377.
[44] J.T. Herron, J. Phys. Chem. Ref. Data 17 (1988) 967–1026.
[45] C. Breheny, G. Hancock, C. Morrell, Phys. Chem. Chem. Phys. 2 (2000) 5015–5112.
[46] L. Ley, J. Masanet, F. Caralp, R. Lesclaux, J. Phys. Chem. 99 (1995) 1953–1960.
[47] G.A. Skorobogatov, O.N. Slesar, N.D. Torbin, Vestn. Leningr. Univ. Ser. Fiz. Khim. 1 (1988) 30–37.
[48] J.C. Amphlett, E. Whittle, Trans. Faraday Soc. 62 (1966) 1662–1667.
[49] T.N. Bell, K.O. Kutchke, Can. J. Chem. 42 (1964).
[50] M.J. Rossi, J.R. Barker, D.M. Golden, J. Chem. Phys. 71 (1979) 3722–3726.
[51] T.L. Andreeva, S.V. Kuznetsova, A.I. Maslov, I.I. Sobelman, V.N. Sorokin, High Energy Chem. 6 (1972) 368–372.
[52] J.W. Bozzelli, M. Kaufman, J. Phys. Chem. 77 (1973) 1748.
[53] D.B. Atkinson, J.W. Hudgens, A.J. Orr-Ewing, J. Phys. Chem. A 103 (1999) 6173–6180.
[54] R.F. Delmdahl, S. Ullrich, K.-H. Gericke, J. Phys. Chem. A 102 (1998) 7680–7686.